IVYSPRING INTERNATIONAL PUBLISHER

Theranostics

2019; 9(24): 7298-7312. doi: 10.7150/thno.38091

Research Paper

Thermal monitoring during photothermia: hybrid probes for simultaneous plasmonic heating and near-infrared optical nanothermometry

Marta Quintanilla[1,*,✉], Isabel García[1], Irene de Lázaro[2,*], Rafaela García-Alvarez[1,2], Malou Henriksen-Lacey[1], Sandra Vranic[2], Kostas Kostarelos[2], Luis M. Liz-Marzán[1,3,✉]

1. CIC biomaGUNE and CIBER-BBN, Paseo de Miramón 182, 20014 Donostia-San Sebastián, Spain
2. Nanomedicine Lab, Faculty of Biology, Medicine & Health and National Graphene Institute, The University of Manchester, AV Hill Building, Manchester M13 9PT, UK
3. Ikerbasque, Basque Foundation for Science, 48013 Bilbao, Spain

*Current address: M.Q.: Materials Physics Department, Universidad Autónoma de Madrid. Avda. Francisco Tomás y Valiente, 7. 28049, Madrid, Spain. I.d L.: 1. Wyss Institute for Biologically Inspired Engineering at Harvard University, Cambridge, MA 02138, USA, 2. John A. Paulson School of Engineering and Applied Sciences, Harvard University, Cambridge, MA, USA

✉ Corresponding authors: marta.quintanilla@uam.es; llizmarzan@cicbiomagune.es

Received: 2019.07.02; Accepted: 2019.08.20; Published: 2019.09.25

Abstract

The control of temperature during photothermal therapy is key to preventing unwanted damage in surrounding tissue or post-treatment inflammatory responses. Lack of accurate thermal control is indeed one of the main limitations that hyperthermia techniques present to allow their translation into therapeutic applications. We developed a nanoprobe that allows controlled local heating, combined with *in situ* nanothermometry. The design of the probe follows a practical rationale that aims at simplifying experimental requirements and exploits exclusively optical wavelengths matching the first and second biological windows in the near-infrared.

Methods: Hybrid nanostructures were chemically synthesized, and combine gold nanostars (photothermal agents) with $CaF_2:Nd^{3+},Y^{3+}$ nanoparticles (luminescent nanothermometers). Both components were simultaneously excited in the near-infrared range, at 808 nm. Following the goal of simplifying the thermal monitoring technique, the luminescent signal was recorded with a portable near-infrared detector. The performance of the probes was tested in 3D spheroids from a human glioblastoma (U87MG) cell line. The location of the beads within the spheroids was determined measuring Nd^{3+} emission in a commercial Lightsheet microscope, modified in-house to be able to select the required near-infrared wavelengths. The temperature achieved inside the tumor spheroids was deduced from the luminescence of Nd^{3+}, following a protocol that we developed to provide reliable thermal readings.

Results: The choice of materials was shown to work as an optically excited hybrid probe. Depending on the illumination parameters, temperature can be controlled in a range between 37 °C and 100 °C. The near-infrared emission of nanothermometers also allows microscopic tracking of the hybrid nanostructures, confirming that the probes can reach deeper into the spheroid mass. We observed that, application of optical thermometry in biological environments requires often neglected considerations, since the optical signal changes along the optical path. Accordingly, we developed data analysis protocols that guarantee reliable thermal readings.

Conclusions: The prepared hybrid probes enter 3D tumor spheroids and can be used to kill them through photothermal effects, while simultaneously measuring the local temperature *in situ*. We show that luminescent thermometry in biomedical applications requires the development of protocols that guarantee accurate readings. Regarding photothermal treatments, we observe a sharp thermal threshold at around 55 °C (for 10 min treatments) that separates high survival ratio from complete cell death.

Key words: photothermal therapy, nanothermometry, plasmonic heating, brain cancer, luminescence sensing, near-infrared

Introduction

Cells and most bacteria can only live and grow within a limited temperature range, often around 37 ^{o}C. Differences of just a few degrees can readily lead to metabolic changes. Indeed, evolution in animals has shaped mechanisms to increase body-temperature by 1 to 4 ^{o}C in response to inflammatory situations. This is manifested as high body temperature ('fever' in warm-blooded species) and has been shown to help increase survival in certain pathological conditions [1]. Indeed, when artificially triggered, this mild level of heating has been exploited as an adjuvant setting to improve the success of certain cancer treatment strategies [1, 2]. If elevated temperatures are achieved locally, cells start to get damaged, mainly due to protein denaturation [3]. This limitation in the survival thermal range can be seen as an opportunity when it comes to developing medical therapies that require killing biological entities such as cancer cells or even bacteria. Such treatments are known as hyperthermal, and the elevated temperatures can be set above 45 ^{o}C, whereas ablation therapy would require temperatures above 70 ^{o}C.

Hyperthermia can be pursued in different ways to achieve a therapeutic effect, particularly seeking a treatment against cancer. For instance, early assays in the late XIX century studied the administration of bacteria to create an infection that would naturally trigger a fever response [4]. Most current options emerged following the synthesis of nanomaterials that can transform an external stimulus into heat and can be selectively placed in the tumor area. Particles made of those materials appear as particularly suitable candidates to trigger localized heating, even in deep tissue if the stimulus can penetrate through the body. The hyperthermia technique was first demonstrated using magnetic nanoparticles, which would release heat upon application of an alternating magnetic field [5]. More recently, nanoparticles that can release heat under optical excitation have also been developed, leading to so-called photothermal therapy. This raised an ongoing debate on the suitability of each type of thermal therapy depending on the disease (on tumor location, for instance) [6]. Although photothermal nanoparticles can be made of a wide variety of materials, including quantum dots, lanthanide-doped nanoparticles or carbon dots, the highest heating efficiencies have been achieved by using gold-based nanoparticles [2, 7].

In all cases, due to the rather uncontrolled distribution of the nanoparticles within biological tissue and the heterogeneity of this environment, it is hard to achieve an accurate control of the temperature reached during the treatment. Actual thermal information of the treated area is required to design successful treatments that can kill the tumors while preserving the surrounding environment. This is especially important when one considers the two main mechanisms of cell death, apoptosis and necrosis, which can be tuned through small temperature changes [8]. It is however key, to control the precise cell death mechanism, because it strongly affects the way the body reacts to the treatment, as e.g. necrosis may trigger inflammatory processes [9]. Indeed, based on these considerations, lack of temperature control has been quoted as the main limitation of current hyperthermal probes [2, 10, 11].

Various techniques have been recently developed to measure temperature within micrometer sized areas [12, 13]. However, measuring temperature during hyperthermal treatment holds strong limitations regarding the selection of thermometry techniques that can be applied. First of all, non-contact techniques should be used, aiming for a minimally invasive therapy. Within this category, the available strategies that can work in the complex biological environment are mainly based on luminescent molecules or nanoparticles [12]. Second, not every luminescent thermometer would work, as it must be specific for temperature (independent of pH, composition of the environment, etc.) and both excitation and emission wavelengths should fall within the biological transparency windows, where absorption and scattering of light are minimized (first window: 750-950 nm; second window: 1000-1350 nm; third window: 1500-1700 nm) [14]. A suitable selection of excitation and emission wavelengths is therefore of utmost importance [15]. On one hand, scattering compromises the directionality of the excitation light through tissue; on the other hand, absorbance reduces the excitation power and produces unwanted heating along the light path. Moreover, commonly used short wavelength light (UV or blue) is known to have phototoxic effects, which is another good reason to move towards longer wavelengths [16, 17].

The combination of heating and temperature monitoring using nanoparticles is an ambitious goal that aims at extending and facilitating the application of hyperthermal therapy. Few attempts have been made to carry out hyperthermia with materials capable of both heating and emitting a temperature-dependent signal. This is the case for Co/Au and Fe/Au nanodomes, in which temperature is tracked optically through the viscosity-dependent rotation dynamics of the particles in the presence of a weak external AC magnetic field [18]. Also, nanoparticles heavily doped with Nd^{3+} or some types of quantum dots have been explored [19-22]. This approach benefits from the simplicity and robustness of the multifunctional probes, but given their limited

heating efficiency (e.g., compared to gold nanoparticles) they require higher illumination doses to achieve a target temperature. Alternatively, hybrid structures have been proposed, by adding a thermometric capability to the most efficient hyperthermal probes [23-27]. These approaches constitute interesting proof-of-concept experiments, but are limited from the biological application point of view, as none of them fulfills the above listed requisites, including the use of near-IR wavelengths, validity in heterogeneous environments, and often involve complex detection or illumination systems requiring more than one light source.

We present here a hybrid nanostructure that combines plasmonic gold nanoparticles as an efficient optical heater, with a specifically designed nanothermometer based on CaF_2:Nd^{3+},Y^{3+}, which could be developed for *in vivo* applications. Both materials can be excited at the same wavelength, 808 nm, in the first biological window, while the nanothermometer emission is located within the second biological window. Accordingly, the luminescence signal from our nanothermometers also allows tracking and localization of the hybrid structure inside a biological tissue mass. We demonstrate application of the hybrid assemblies by photothermal killing of cancer cells, while recording temperature *in situ*, so that we can determine the thermal resolution they can achieve and define experimental protocols that provide an accurate thermal reading.

Results and Discussion

The selection and measurement of temperature in localized spots is key to controlling photothermal therapy and regulating irradiation doses for each specific treatment. The preparation of a probe that can be optically activated for both heating and temperature monitoring, requires a careful selection of materials for each specific task. Gold nanoparticles were chosen to play the role of heaters, since they are among the materials that most efficiently transform light into heat, while presenting negligible toxicity for human cells [28]. The optimal illumination wavelength for heat production, as well as the heating efficiency, are largely determined by the nanoparticles morphology. Particularly efficient nanostructures comprise anisotropic shapes with sharp edges or pointy features, such as nanotriangles, nanorods or nanostars [29, 30]. On the basis of prior experience, we decided to work with gold nanostars that are resonant at ca. 800 nm, as shown in Figure 1A.

Gold nanostars were prepared by seeded growth, using ascorbic acid as reducing agent and silver nitrate to assist the growth of spikes [31]. The selected particles featured a tip-to-tip diameter of 83 ± 7 nm (See Figure 1B). Colloidal and morphological stability, as well as negative surface charge (required for subsequent fabrication steps), were achieved by surface functionalization with a thiolated polyethylene glycol (PEG), terminated in a carboxyl group. The heating efficiency of our gold nanostars at the laser wavelength used in photothermal experiments, was calculated to be 74% (For details on these measurements, refer to Section A1 and Figure S1 of the SI). Using the same excitation wavelength, heating efficiencies between 40% and 100% have been measured for gold nanostars of different sizes [29], which leaves those prepared here in the middle of that range.

To select our thermometric material, we placed emphasis on the requirement of working within the biological transparency windows, but also on the spectral compatibility with the heaters, the accuracy of the thermal reading and the possibility of retrieving absolute temperature values. Accordingly, we chose CaF_2 nanoparticles doped with neodymium and yttrium as thermometers, which can be readily synthesized following a recently reported hydrothermal method [32], yielding cubic particles with 11 ± 3 nm side length (Figure 1C). As prepared, particles are protected by citrate, and hence stable in aqueous solution. In CaF_2:Nd^{3+},Y^{3+} particles, Nd^{3+} is the active ion absorbing light (at 808 nm) and featuring a strong emission band at 1050 nm (as shown in Figure 1D), whereas Y^{3+} is added to break energy migration paths between Nd^{3+} ions, which would otherwise quench the emission intensity. Following a previously reported discussion on this matter [33], we selected doping concentrations of [Nd^{3+}] = 1%, [Y^{3+}] = 15%. These nanoparticles can be excited at the same wavelength as our gold nanostars (see the energy diagram scheme in Figure 1D). Thus, both pursued functionalities, heating and thermal monitoring, can be triggered using a single light source. It is also noteworthy that lanthanide ions as dopants typically present characteristic narrow emission lines, which are easy to differentiate from any other signal from organic molecules present in biological tissues. The lanthanide emission additionally features a large Stokes shift, thereby minimizing the absorption of emitted light by nearby gold nanostars. These nanoparticles constitute a ratiometric thermometer based on the emission peak at 1050 nm. When Nd^{3+} ions are embedded inside a crystal, the electromagnetic field created by the surrounding atoms breaks the degeneracy of the $^4F_{3/2}$ state (see scheme in Figure 1D), which gets divided into two sublevels, R_1 and R_2. Consequently, the emission at 1050 nm is actually an overlap of the

emissions from these two sublevels. Given the small energy gap between R_1 and R_2 their electronic populations, and hence their emissions, are thermally linked. If we call I_1 the emission intensity from R_1, and I_2 the emission intensity from R_2, since the ratio between both intensities is given by a Boltzmann distribution, it can be written as:

$$\frac{I_2}{I_1} = Bexp\left(\frac{-\Delta E}{k_B T}\right) \rightarrow \ln\left(\frac{I_2}{I_1}\right) = lnB - \frac{\Delta E}{k_B T} \qquad (1)$$

where B is an experimental constant, k_B is Boltzmann's constant and ΔE is the energy gap between R_1 and R_2. By applying logarithms to both sides of the equation, the relationship on the right is obtained, which allows us to plot the intensity ratio versus de inverse of temperature in the form of a linear function with slope $-\Delta E/k_B$. The main advantage of this type of thermometers is that the ratiometric technique is in itself a self-referenced method, thus providing absolute temperature measurements. Besides, the intensity ratio does not depend on the excitation power or on the concentration of particles, thereby minimizing the sources of error during thermal reading.

In Figure 1D we marked with two dashed squares the part of the spectrum to be integrated to retrieve I_1 (red) and I_2 (green), the limiting wavelength being 1057 nm [33]. Thermal calibration can be performed by measuring the emission from a colloidal dispersion of the particles at various set temperatures. It is important for the accuracy of the calibration to use a low laser power, so as to minimize uncontrolled optical heating of the environment. We thereby obtain a plot such as that shown in Figure 1E. Following eq. (1) we can get a linear fit (blue line and equation within the graph), yielding a value of ΔE equal to 58 cm^{-1}, which is consistent with previously reported values for the same doping concentration [33]. Once the precise relationship between intensity ratio and temperature has been established for our nanoparticles, the opposite experiment can be performed to calculate temperature values from emission spectra.

We therefore prepared gold nanostars that could heat their nearby environment, as well as $CaF_2:Nd^{3+},Y^{3+}$ nanoparticles to measure temperature, both upon excitation at 808 nm. Co-localization of the components for photothermal experiments was ensured by co-assembly into hybrid structures. It should be noted that both nanostars and nanothermometers carry a negative surface charge, due to the selection of surfactants (carboxyl terminated PEG for nanostars, featuring a zeta potential of -25 mV, and citrate for nanothermometers, with a zeta potential of -7 mV), so they can be electrostatically linked onto positively charged surfaces. As a proof-of-concept, we chose polystyrene beads as a colloidal support [34]. The selected beads had an average diameter of 500 nm and were functionalized with amino groups, thereby featuring a positive surface charge, indicated by a zeta potential value around +40 mV (Figure S2).

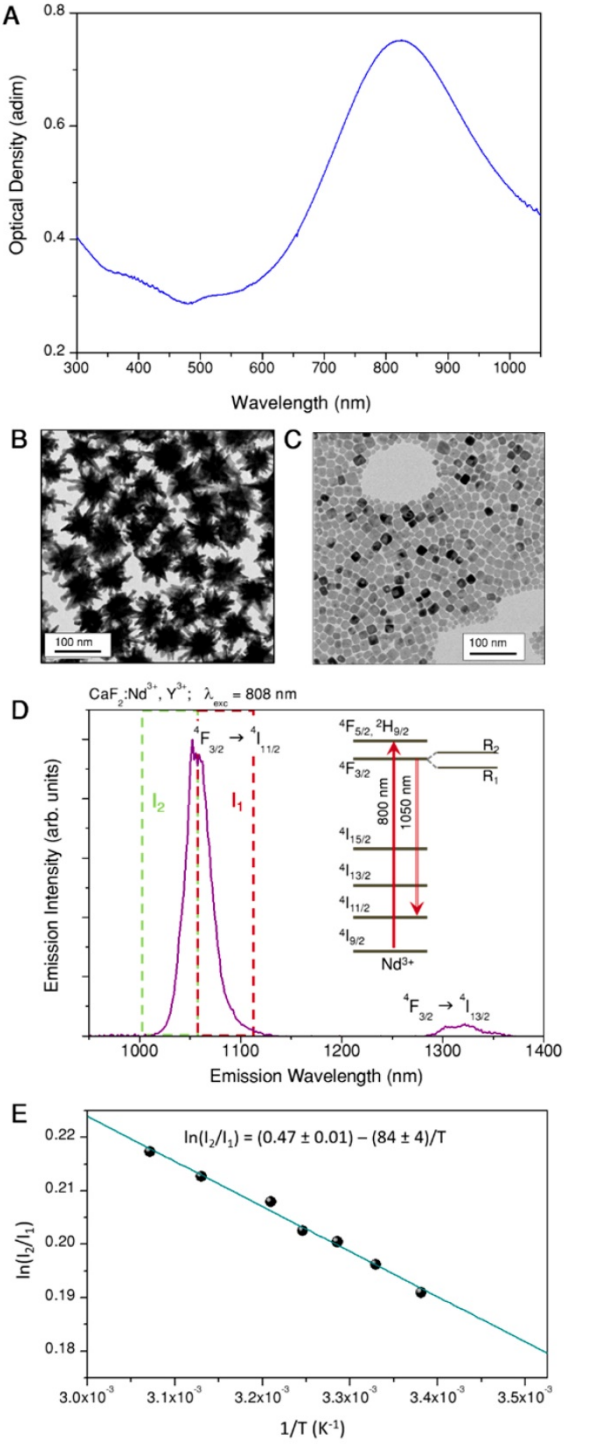

Figure 1. A) Extinction spectrum of gold nanostars. B) Representative TEM image of gold nanostars. C) Representative TEM image of $CaF_2:Nd^{3+},Y^{3+}$ nanoparticles. D) Emission spectrum under 808 nm excitation of $CaF_2:Nd^{3+},Y^{3+}$ nanoparticles, used as thermometers; a partial scheme of Nd^{3+} energy states is included in the inset; green and red dashed lines frame the two emission ranges used for ratiometric thermometry. E) Thermal calibration curved obtained by dividing the area covered by the emission intensities in the two highlighted regions (D).

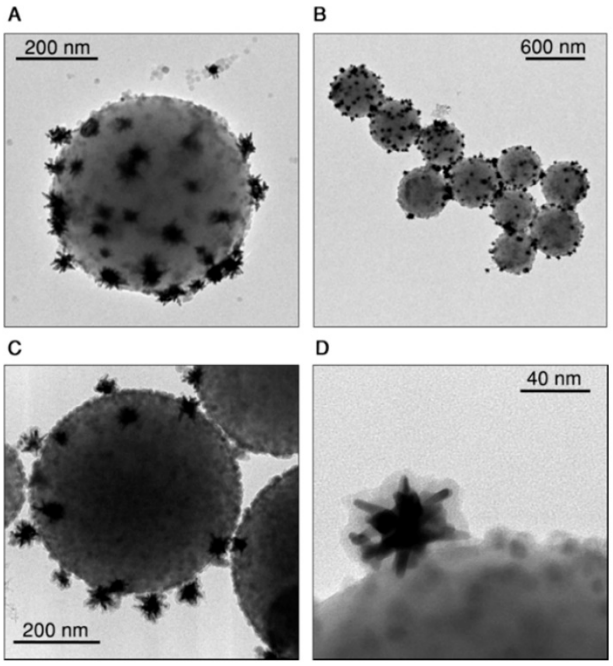

Figure 2. Representative TEM images of assembled beads before (A, B) and after (C, D) silica coating.

Upon electrostatic self-assembly by subsequent addition of CaF_2 nanoparticles and gold nanostars to a dilute dispersion of beads, hybrid nanostructures were obtained as shown in Figure 2A and B (supplementary images are provided in Figures S3, S4 and S5 of the SI). The gradual modification of the colloidal beads was confirmed by monitoring changes in zeta potential, which became negative (-18 mV) upon addition of the nanoparticles (Figure S2) and in the hydrodynamic diameter, which shifts from 515±6 nm to 750±20 nm (Figure S2). The TEM images show few free nanoparticles (gold nanostars and CaF_2) next to the assemblies, even after four washing centrifugation steps. We concluded that these free particles likely derive from sample preparation for TEM (see short discussion in the SI, Figure S6). To prevent potential disassembly, which may also occur when the sample is placed in biological environments, we coated the hybrid probes with a thin shell of silica. We employed the standard Stöber method by adding tetraethyl orthosilicate (TEOS) to a dispersion of beads in a water/isopropanol mixture (H_2O:IPA = 1:1.8) containing ammonia at pH 9 [35, 36]. By TEM analysis we measured a silica shell thickness around 7 nm, and confirmed homogenous coating of both gold nanostars and CaF_2 nanoparticles on the beads surface (Figure 2C,D, and S7, SI). The hydrodynamic diameter increased up to 830 ± 30 nm as observed in DLS, with a further shift toward negative zeta potential, down to -40 mV (Figure S2). After silica coating, no free nanoparticles were found in TEM images (Figures 2C,D and S7, SI).

The emitting and heating properties of the assemblies were tested in an aqueous dispersion (1 mL, 0.02 wt.%) homogeneously illuminated with an 808 nm laser beam and with a thermal camera monitoring the upper surface of the suspension (Figure 3A). Figure 3B shows thermal images obtained upon illumination at three different power densities, demonstrating the heating abilities of the assemblies. The beads were further concentrated and redispersed in 200 µL (resulting concentration 0.1 wt.%) of cell culture medium, to perform four heating and cooling cycles as shown in Figure 3C, in which the illumination laser was switched on and off to confirm the reproducibility of the achieved temperature. The heating efficiency of the hybrid beads ranged between 17% and 25%, depending on the nanostar loading. This decrease in heating efficiency, as compared to the gold nanostars alone, was due to light scattering from the beads, which reduced the transparency of the sample. However, the final achieved temperature will depend mainly on the number of nanostars present under the beam and their spatial distribution.

The emission of CaF_2:Nd^{3+},Y^{3+} was measured after incorporating the nanoparticles onto the assemblies and dispersed in cell culture media (Figure 3D, black line). A comparison of the spectrum to that from dispersed, bare CaF_2:Nd^{3+},Y^{3+} nanoparticles in water (Figure 3D, green line) shows that, when the nanoparticles are included in the hybrid beads, an additional emission band is observed at longer wavelengths (1070 to 1150 nm). This band was found to correspond to Raman scattering from water (the Raman spectrum of pure water is also shown in Figure 3D, orange line). Raman scattering is typically less intense than luminescence, but it should be noted that here a large number of water molecules can contribute to the band. In addition, the signal from water molecules in close proximity to Au nanostars may be enhanced when excited at the plasmon resonance wavelength due to the surface enhanced Raman scattering (SERS) effect [34, 37]. Having identified the origin of this band, as well as its shape, we can now deconvolute it from the measured spectra because it is weakly dependent on temperature within the overlapping region [38, 39]. Also, for the sake of accuracy, we also narrowed down the wavelength range in which the Nd^{3+} emission band was integrated, to further avoid interferences from the Raman scattering band of water (I_2 is the integrated area between 1014 nm and 1057 nm, I_1 is the area between 1057 nm and 1074 nm). Further details regarding the protocol followed to analyze the recorded spectra can be found in the SI, Section B3i.

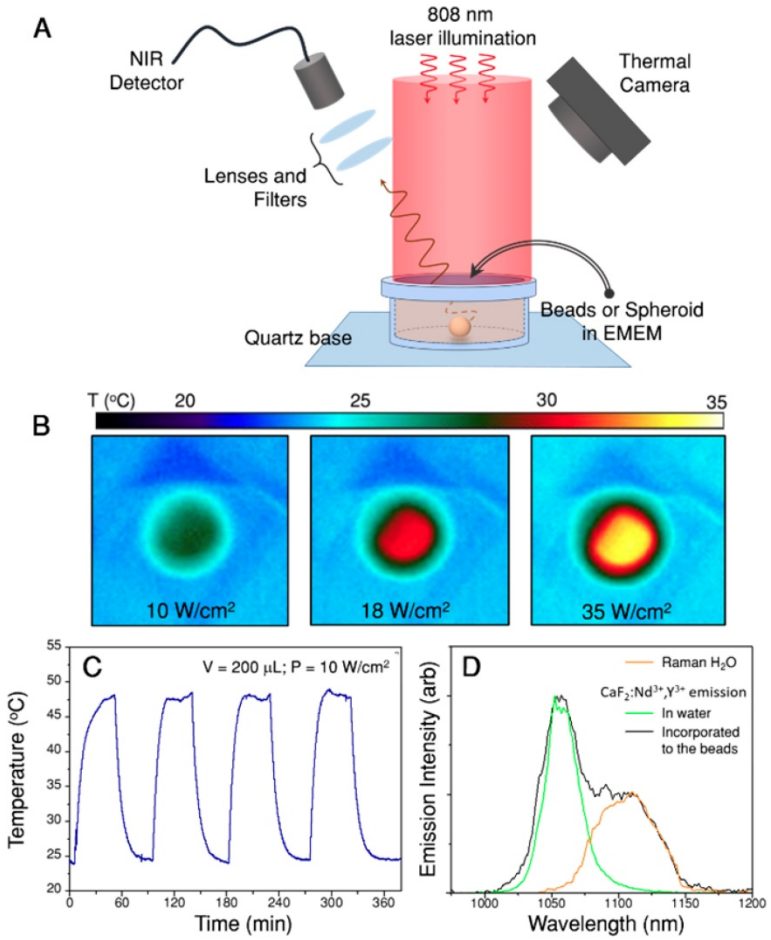

Figure 3. Heating and emitting properties of hybrid beads containing Au nanostars and CaF_2:Nd^{3+},Y^{3+} nanoparticles. A) Experimental set-up used to illuminate the samples and record their luminescence while monitoring the temperature of the solution with a thermal camera. B) Thermal camera images upon illumination of 1 mL of beads solution (0.02 wt.%) with three different powers. C) Heating and cooling cycles of 200 µL (0.1 wt.%) in cell medium, EMEM. D) Emission spectrum recorded in the emission range of Nd3+ upon 808 nm illumination of a 200 µL dispersion in EMEM. The spectrum shows the expected emission of Nd3+ and an additional contribution from Raman scattering by water molecules.

Tracking hybrid beads in 3D *in vitro* tumor models

As shown above, apart from the excitation power, several environmental parameters can affect photothermal efficiency (e.g. heat dissipation of the environment, beads concentration). A realistic picture of the actual capabilities of the hybrid structures and their potential performance to monitor photothermal therapy requires their incorporation into representative cell models. We selected 3D tumor spheroids, as they better represent the real physiological and environmental features of the tumor, as compared to 2D cell monolayers, including the penetration of particles within the tumor and the resistance of cells to thermal shock [8]. Since our multifunctional assemblies can be tracked via luminescence imaging, it should be possible to obtain information on the distribution of the probes inside the 3D model.

Spheroids were prepared using the U-87MG human glioblastoma cell line. Our protocol uses a starting number of ca. 5000 cells/spheroid in 200 µL of cell media (Day 0). Two days later they have become stable spheres with sizes around 500 µm. At this point the hybrid beads were added to the cell culture medium and incubated to allow internalization for 48 hours, at which point the spheroids presented a diameter of ca. 600 µm (see size and shape evolution of spheroids in the SI, Figure S8).

The location of beads in cells and spheroids was monitored through Nd^{3+} luminescence, using a Lightsheet microscope modified so it can specifically record the emission band at 1050 nm, particularly advantageous to improve the penetration depth [15]. Figure 4 shows a representative set of images measured for different spheroids. In these images, the red color represents the emission from Nd^{3+}, while blue color depicts DAPI, which was used to label cell nuclei. Through high magnification images in the area close to the edges of a spheroid, where a better spatial resolution can be obtained, it is observed that both signals are not co-localized. Indeed, Nd^{3+} emission is observed surrounding DAPI emission, which points

towards the location of the beads in the cell cytoplasm (Figure 4A).

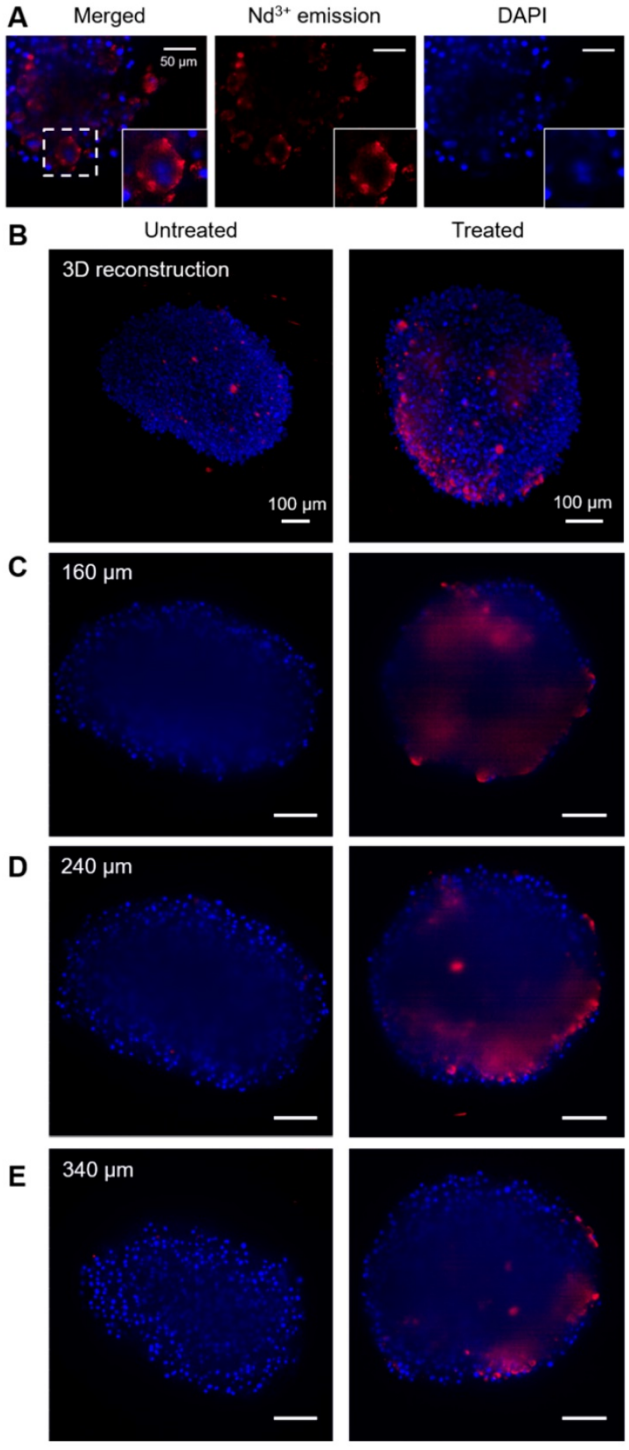

Figure 4. Fluorescence images of spheroids. In all images blue color stands for DAPI (cell nuclei) and red stands for Nd^{3+} emission. A) Images of the surface of a treated spheroid (150 µg/mL), showing Nd^{3+} emission apparently located in the cytoplasm. Below, two columns of images are shown, related to an untreated spheroid (left) and a spheroid treated with beads (100 µg/mL). A 3D reconstruction of the spheroid (B) and several cross-sections of each spheroid (C, D, E) are displayed.

Regarding bead distribution within the whole spheroid, Figure 4B-E shows representative images of the full structures. First, a 3D reconstruction built by stacking around 500 cross-sections is presented (Figure 4B), followed by cross sections at different depths of the same spheroids (Figure 4C-E). In every case, the image in the left column corresponds to a non-treated spheroid and is shown as a reference, whereas the spheroid in the right column was treated with 100 µg/mL of hybrid beads. All images were taken under exactly the same conditions for a fair comparison. In order to interpret the images, it must be taken into account that DAPI emits in the visible range, while Nd^{3+} does in the near-infrared, within the second biological window. Accordingly, it is expected that the signal from DAPI is partially lost due to absorption when it has to travel through the spheroid, while the Nd^{3+} signal should remain largely unaltered [15]. It should be noted that, the reference spheroid (left column) does not display any signal in the Nd^{3+} luminescence range inside the spheroid (above 850 nm). We do observe however some NIR emitting objects outside of the untreated spheroid, which are commonly seen in all samples and can be assigned to small fibers present in PBS or agar, used to mount the samples. As they mainly appear outside the spheroids and present a distinctive shape, these features can be easily identified. Accordingly, we can confirm that the observed NIR luminescence inside treated spheroids stems solely from Nd^{3+}, and that the hybrid beads are entering the spheroids down to at least 200 µm. It is worth noting that the spatial resolution and intensity of DAPI luminescence is partly lost inside the spheroid due to scattering and absorption along the light path. Luminescence from Nd^{3+} is also affected, especially in terms of spatial resolution. However, its emission intensity can be clearly detected inside the spheroid, likely because the selected wavelength matches the second biological window.

Before proceeding with photothermal experiments, we studied the viability of U87MG spheroids when exposed to different concentrations of hybrid beads, to determine the most suitable concentration range. For these experiments, the CellTiter-glo 3D test (Promega), which uses ATP as cell viability indicator, was applied. The results are plotted in Figure 5A, in which the concentrations refer to hybrid beads diluted in EMEM (200 µL). However, we determined by inductively coupled plasma-mass spectrometry (ICP-MS) measurements that only 2-8% of the beads were actually internalized in the spheroids. Such a low internalization efficiency is likely due to a large percentage of beads not even reaching the spheroid, which lies at the center of the well. Still, minor toxicity is observed in all samples, from which 100 µg/mL was determined as the upper limit to be used. Regarding the initial proportion of

living and non-living cells in the spheroid prior to any photothermal treatment, we also analyzed the possible existence of a necrotic core, as often happens in 3D cell models [40]. In our case, necrotic cores were not identified within the working period (see SI, Figure S10). Finally, aiming at setting the parameters for photothermal treatment (time and laser power), we tested the viability of spheroids at different illumination powers and times, in the absence of beads (Figure 5B,C). We found that the effect of the laser in the selected power range is negligible within the treatment time (10 min). The observed variability, up to 15 min, was also within experimental error.

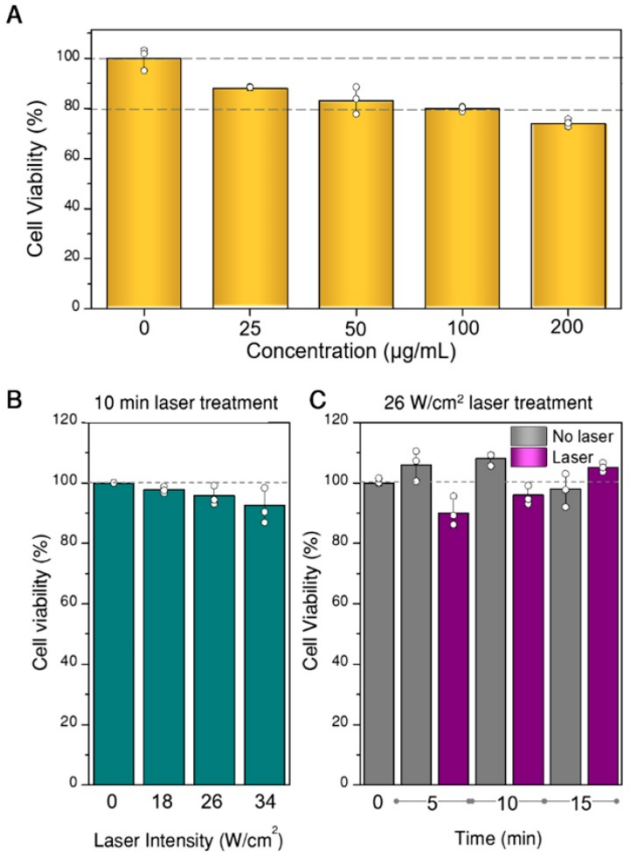

Figure 5. Viability of spheroids as a function of the concentration of hybrid beads in cell culture media (A), of laser power density at 808 nm for 10 min illumination (B), and of illumination time at 26 W/cm² power density (C). All experiments were done in triplicate, data are shown as mean and standard deviation.

Thermometer pre-calibration

With all this information at hand, we can now start designing photothermal treatments while simultaneously monitoring temperature. However, accurate temperature readings require recalibration of $\ln(I_2/I_1)$ vs. T [33, 41]. In eq. (1), ΔE is independent from the external environment due to electrical shielding of 4*f* orbitals. However, B is a correction parameter related to detected differences in the emission intensities, and thus it is only constant for a fixed experimental scenario. Indeed, changes may arise from the selection of light detector, or the presence of a potential absorber in the light path toward the detector [42]. This event is likely to occur in practical therapies, as light will travel through non-transparent media, such as cells, blood, culture media, etc. In our case, gold nanostars will also play a role as their absorbance at the emission wavelength cannot be neglected (see Figure 1A).

To overcome this hurdle, thermal measurements should be preceded by a recalibration step to determine ln(B) under the exact experimental conditions. This preliminary step has been formerly done by measuring the emission from the nanoparticles at different illumination powers [33, 41]. Since heaters are present, each power will produce a distinct temperature, following a linear dependence. At zero power the system is at room temperature, which is known, so we can safely determine ln(B) through eq. (1) by fitting $\ln(I_2/I_1)$ data recorded at different powers to a straight line.

We first tested the protocol in the dispersions of beads shown in Figure 3C, which can also be accurately monitored with the thermal camera. Following the explanations above, the initial step comprised measuring luminescence spectra at different illumination powers and processing the spectra to obtain $\ln(I_2/I_1)$ values. These values were then used to recalibrate ln(B), which was found to be 0.443 in this case (Figure S13A). Introducing this number in eq. (1) we can now calculate the temperature that corresponds to each $\ln(I_2/I_1)$. The obtained results are shown in Figure 6A, together with the temperature recorded by the thermal camera. Both thermal measurements were found to be in agreement, with differences typically below 1.5 ºC, which validates the protocol.

It is now possible to apply this method to investigate the thermal evolution of the solutions after switching on the illumination, i.e. starting at room temperature, until thermal equilibrium was reached. Figure 6B presents the thermal data over time obtained through nanothermometry (blue dots) and with the thermal camera (grey line). As expected, temperature follows an exponential growth until reaching thermal equilibrium, in both cases at 48 ºC. Indeed, the trend is largely the same, regardless of the method used to measure temperature. The only difference is that equilibrium is reached slightly earlier according to the nanothermometers (see exponential fit, i.e. the dashed blue line). Definitive conclusions on the origin of this slight discrepancy would require a better accuracy than that achieved here. However, it can be hypothesized that the differences between both techniques play a role, likely

due to the fact that nanothermometers are always located close to the gold nanostars, while the thermal camera measures the average temperature in the whole area covered by each pixel.

To apply this recalibration method to 3D cell models, the set-up in Figure 3A was kept the same; only the solution of beads was replaced by a spheroid immersed in cell medium (EMEM). As a consequence, the thermal camera only records the temperature on the surface of EMEM, and it cannot directly monitor the spheroid itself. Recalibration of ln(B) was first performed using a starting sacrificial tumor spheroid, which was illuminated at different laser powers. The obtained values of $\ln(I_2/I_1)$ vs. power are plotted in the inset of Figure 6C, as the average of three different spectra, with error bars representing the corresponding standard deviations. In principle, we expected that the intensity ratio would increase linearly with the illumination power, due to photothermal heating. This is confirmed in Figure 6C, but only for the lower excitation powers considered. However, for laser powers above 2700 mW an apparent thermal decrease was found. Using these first data to recalibrate ln(B), a new value of 0.444 was obtained, i.e. slightly below the one measured for $CaF_3:Nd^{3+},Y^{3+}$ in water, and almost equal to that obtained for beads in EMEM (further details on this calculation are given in Section B3ii and Figure S14 of the SI). This suggests the idea that the change in ln(B) is mainly due to gold nanostars and EMEM, and not so much to the presence of cells. This new ln(B) value was used to calculate the corresponding temperatures in the full power range, as shown in the main graph of Figure 6C.

According to these results, the temperature increases up to 104 ^{o}C, then reaches a plateau and decreases at powers above 2700 mW (38 W/cm^2). This behavior is consistent with a water-based environment like the cell culture medium, in which evaporation starts consuming energy at around 100 ^{o}C. The following decrease of temperature might be related to two simultaneous effects. The first one is the potential reshaping of gold nanostars [43], whose tips have been shown to become more rounded at high temperatures, thereby triggering a blue-shift of the near-infrared plasmon resonance. This would have detrimental effects, both on the absorbance of the sample at 808 nm and on its heating efficiency. Absorbance measurements of gold nanostars treated at 100 ^{o}C (Figure S15) confirmed that after 10 minutes the plasmon shift was around 15 nm, and absorbance at 808 nm decreased by 6%. As the experiment was done keeping each laser power for 3 min, the actual time at this temperature is shorter than that. Accordingly, reshaping might only be a partial contribution to the temperature decrease. The second possible reason is the reduction of collective heating effects [44, 45], which are probably strong here. In other words, the spheroid may undergo expansion and fracture, resulting in a reduction in the density of hybrid beads. As the final temperature is the sum of the contributions by all heaters, this morphological change results in a delocalization of the hot area and a temperature decrease around the nanothermometers. These findings were supported by visual observations during the experiment, with the aid of a portable microscope. Three selected images are shown in Figure 6D-F, in which two principal effects are observed: creation of bubbles when the medium started evaporating (Figure 6E), and expansion and fracture of the spheroid after complete irradiation (Figure 6F).

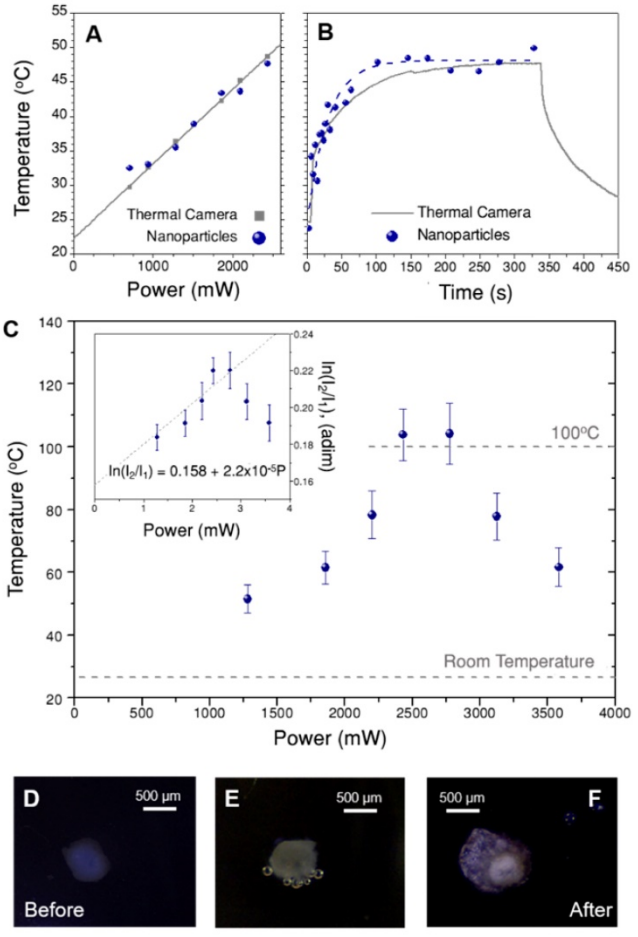

Figure 6. A) Temperature obtained for the solution of beads illuminated at different powers, measured both with a thermal camera (grey squares) and by nanothermometry (blue dots). B) Heating curve of the dispersion of beads over time. At time zero, the laser was switched on at 2400 mW. The dashed blue line is an exponential fit to the data. Note that figures A and B have the same vertical scale. C) Temperature measured at different excitation powers in a spheroid treated with hybrid beads (70 µg/mL), calculated by nanothermometry. The inset shows the same data as intensity ratio, i.e., prior to applying the calibration. Three representative images of the spheroid are added below, to show its appearance, D) before the treatment, E) after 3 min illumination at 2500 mW (35 W/cm^2) and F) at the end of the treatment. Please note that the spheroid may move and rotate due to the thermal gradient created in the well.

The described protocol yields temperature values that are consistent with the effects observed on the spheroids. However, it may follow from this discussion that a recalibration of ln(B) would be needed each time any parameter is changed in the sample or its environment, thus requiring a new sacrificial spheroid. To avoid that, we tested an alternative strategy based on the dependence of temperature with time during illumination. It is clear from Figure 6B that temperature increases exponentially over time, as dictated by thermal equilibration equations [46]. At sufficiently short time points, this trend can be approximated to a straight line. The proposed time-based strategy comprises recording emission spectra within the starting time range and fitting the obtained values to a straight line. This fit is related to ln(B) in the same way as the power trend in Figures 6A and C, assuming room temperature at time zero (See section B3ii of the SI and Figure S13B for a detailed discussion on the method). The main limitation here is related to our time resolution during the experiments (between 30 and 50 s for the spheroids), which limits the number of points we can use in the fit. However, using two spheroids, identical to that in Figure 6C, to test this new strategy, we estimate that the time-based protocol yields differences in ln(B) below 2% (exact obtained values are 0.443 and 0.451). It can thus be considered a fair approximation, and we can use it in subsequent photothermal experiments, avoiding the need for extra samples for recalibration. Further details on ln(B) calculations are given in the SI (Section B3ii and Figure S14).

Photothermia and *in situ* temperature determination

In order to study the local temperature in tumor spheroids during illumination and the related cell survival rate, four sets of samples were prepared. Each set was treated with a different concentration of hybrid beads: 70 µg/mL, 43 µg/mL, 20 µg/mL and no heaters (CaF_2:Nd^{3+},Y^{3+} nanoparticles alone were added to the latter set to locally measure temperature). During the experiments, two different excitation powers, 26 W/cm² and 31 W/cm², were used and each experiment was carried out in triplicate, to determine the statistical error. In every case, the treatment time was fixed to 10 min.

The recorded thermal data after transforming intensity ratios into temperature are plotted in Figure 7. The time evolution of temperature (Figure 7A) consistently follows an initial fast increase until thermal equilibrium is reached at around 100s. These data were used to determine ln(B). After this time, temperature remained stable for most of the samples. The only deviation was found for spheroids treated under the most extreme conditions (70 µg/mL, 31 W/cm², wine-colored data in Figure 7A), at which the boiling point of water is likely reached prior to cooling due to expansion of the spheroids after treatment. To a lesser extent, some expansion was also observed for spheroids reaching temperatures above 55 ºC (Figure 8). In the time range at which thermal equilibrium was reached (above ~100s), the observed thermal fluctuations can be considered as a measurement of the thermal resolution for each experiment. Since thermal resolution is limited by the signal-to-noise ratio in the spectra, it depends again on excitation power and beads concentration. We found typical values between 3 ºC and 4 ºC, but it could be as high as 9 ºC for the sample with the lowest concentration of beads and the lowest excitation power. For the sake of clarity we did not add such strongly fluctuating data to Figure 7A, and considered this experiment as a limiting situation for the validity of the thermometry method. These results can be found in the SI (Figure S16).

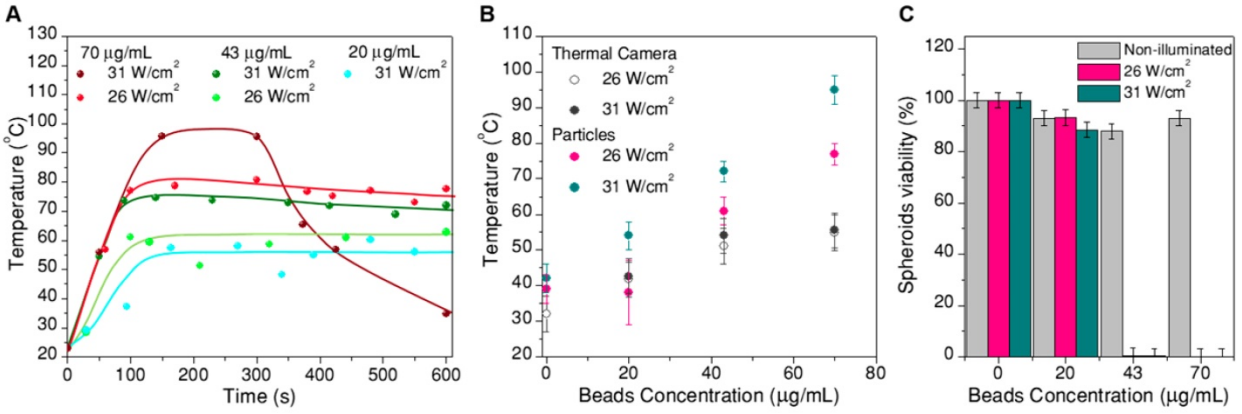

Figure 7. A) Temperature measurements inside spheroids during photothermal treatment: thermal evolution over time, for treatments at different excitation powers and concentrations of hybrid beads. B) Average temperature at thermal equilibrium for each treatment, compared to the temperature determined by a thermal camera. C) Viability of the spheroids at 24h after photothermal treatment

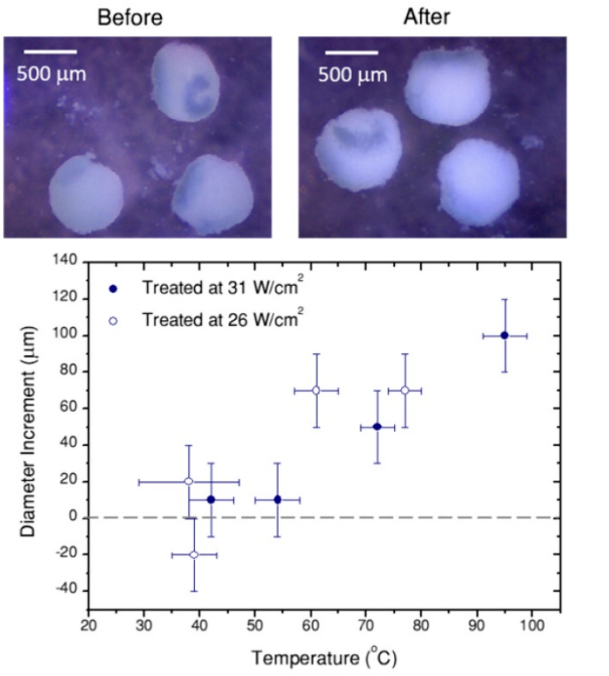

Figure 8. Portable optical microscope pictures of spheroids before and after a laser treatment (10 min, 26 W/cm², 70 µg/mL hybrid beads). Note that probably due to thermal currents, spheroids move during the treatment. In the graph, their diameters before and after the treatment are plotted versus the temperature achieved in the treatment. Error bars correspond to the thermal resolution and the standard deviation of size.

Plotted in Figure 7B is the average temperature within the equilibrium state, where the error bar is given by the thermal resolution (in this case the lowest concentration, lowest excitation experiment is included). The data clearly show that the reached temperature consistently increases with the concentration of beads and with laser power, as expected. We also added to this plot the temperature measured by a thermal camera (with its corresponding 5 ºC accuracy, as given by the commercial brand). The temperature measured by the particles is consistently higher than that measured by the camera, in agreement with the sensitivity of the particles toward local temperature in the spheroid, while the camera monitors the temperature at the surface of the cell medium. This comparison provides a clear idea on the importance of considering local heating for this type of applications.

Finally, Figure 7C shows the cell viability in the spheroid, 24h after photothermal treatment, related to the respective non-treated reference. Correlating these data with the thermal information in Figure 7A,B, we can conclude that local temperatures between 40 ºC and 55 ºC have little or no effect, for a 10 min treatment. Instead, as soon as 55 ºC is surpassed, cells in the spheroid are almost completely dead (viability below 1% for a treatment reaching 61±4 ºC, viabilities below 0.3% consistently determined above 70 ºC. It should be noted that a ±3% statistical error was obtained). This result shows a sharp temperature dependence of cell viability in spheroids, clearly defining a life/death threshold, which in our case was set around 55 ºC. These results are in agreement with previous reports [8] on the viability of PC3 prostate cancer spheroids, in which the authors determined that after similar treatment times the threshold temperature was between 51 ºC and 53 ºC. This might be related to the observed swelling of the spheroid, which happens within the same temperature range (Figure 8). Such a size increase has also been observed in earlier works devoted to hyperthermia treatment, and was ascribed to expansion of the intracellular space [47].

Conclusions and perspective

A hybrid heater/thermometer nanoprobe was designed, comprising gold nanostars and $CaF_2:Nd^{3+},Y^{3+}$ luminescent nanoparticles on a colloidal carrier. Both nanoparticle elements can be excited at the same wavelength, within the first biological window (808 nm), whereas nanothermometers emit within the second biological window (1055 nm). We showed that near-IR emission can be used to track the position of the beads within cell models, by means of a commercial Lightsheet microscope. The same irradiation conditions were subsequently used to measure absolute temperatures *in-situ* inside 3D tumor models. The obtained thermal data were consistently linked to perceptible events occurring to the spheroids, such as bubbling at around 100 ºC, or swelling at temperatures where necrosis was expected. Accurate thermal readings required a pre-calibration step at the same experimental scenario in which the photothermal treatment was to be performed. We determined that this step can be reduced to a linear fit of emission data recorded at short times (<100 s in our experiments), even if only few data could be recorded within this time frame. The time resolution of our thermal experiments was around 30 s, and thermal resolution typically around 4 ºC (though it may vary for different experiments).

This work sets the path toward *in vivo* experiments, but this step would require certain improvements to optimize the hybrid probes e.g. reducing bead size. If novel designs are to be proposed, we would particularly point towards strategies that increase the number of nanothermometers per gold nanostars, to favor their luminescence intensity and reduce time resolution. It should be stressed that gold nanostars have to be slightly (>5 nm) separated from the luminescent nanoparticles to avoid luminescence quenching. Special attention should also be paid to chemical

strategies that provide robust probes and allow surface functionalization. This is particularly important on the way towards clinical applications, to favor the internalization and circulation time of the probes. Also, along the path of clinical translation, illumination doses need to be reduced. In this regard, the present work should be taken as a proof-of-concept, as the volume of the clinical samples and the commonly deep-seated location of tumors within the body must be considered when designing appropriate illuminating and imaging devices, which would definitively affect the required power range.

Materials and Methods

Materials

Hydrochloric acid (HCl, 37%) was purchased from Panreac. Hydrogen tetrachloroaurate trihydrate ($HAuCl_4 \cdot 3H_2O$, ≥99.9%), sodium citrate tribasic dihydrate (≥98%), silver nitrate (AgNO3, ≥99%), L-ascorbic acid (AA, ≥99%) were purchased from Sigma-Aldrich and O-[2-(3- mercaptopropionylamino)ethyl]-O'methylpolyethylene glycol (PEG-SH, Mw 5,000 g/mol) was purchased from RAPpolymere. Amino functionalized polystyrene beads (NP size 483 ± 3 nm) were purchased from IKERLAT Polymers (Lasarte, Spain). All glassware was washed with aqua regia, rinsed 3-fold with milli-Q water and dried before use. Milli-Q water (resistivity 18.2 MΩ·cm at 25 °C) was used in all experiments.

For the synthesis of lanthanide-doped CaF_2 the starting reagents were calcium chloride (≥ 99%, Sigma-Aldrich) and ammonium fluoride (98+%, Acros) as CaF_2 precursors, neodymium chloride (99.9%, Alpha Aesar) and yttrium chloride (99.99%, Alpha Aesar) as lanthanide sources, and sodium citrate tribasic dihydrate (Sigma-Aldrich) as a surfactant. All chemicals were used without further purification, and all experiments were carried out using nanopure water.

Synthesis of gold nanostars

Au nanostars (AuNS) were prepared by a modified seed-mediated growth method to show a plasmon resonance peak at around 800 nm [31]. Briefly, the seed solution was prepared by adding 0.5 mL of a 1 % citrate solution to 9.5 mL of boiling 0.5 mM $HAuCl_4$ solution under vigorous stirring. After 15 min of boiling, the solution was cooled down to room temperature and then kept at 4 °C for long-term storage. The as-synthesized Au nanoparticle seeds had an LSPR maximum at 519 nm. For Au NS synthesis, 50 µL of the citrate-stabilized seed solution was added to 1 mL of $HAuCl_4$ (0.25 mM) solution containing 2 µL of HCl (1.0 M) in a 2 mL glass vial at room temperature, under moderate stirring. Quickly, 10 µL of $AgNO_3$ (3 mM) and 5 µL of ascorbic acid (100 mM) were added simultaneously to the above solution. The solution rapidly turned from light red to greenish indicating the formation of AuNSs. Immediately after synthesis, the solution was stirred with PEG5000-SH (15 molecules/nm^2) for 15 min, washed by centrifugation (6000 rpm, 45 min, 10 °C) and redispersed in water. The used solution had an absorption coefficient of 0.4 cm^{-1} at 400 nm.

Synthesis of Ln^{3+}-doped nanoparticles

CaF_2 doped with a 1% of Nd^{3+} and 15% Yb^{3+} were prepared by a hydrothermal method [32]. The concentration of dopants was selected based on a previous work [33], and is [Nd^{3+}] = 1 mol% and [Y^{3+}] = 15 mol%. The mass of chlorides containing calcium, neodymium and yttrium was calculated to obtain 3.5 mmol of the final material, being 90 mg $NdCl_3$, 160 mg YCl_3 and 432 mg $CaCl_2$. Chlorides were first dissolved in 10 mL of water, and stirred for around 30 min. Then, 5.8 g of sodium citrate in 10 mL of water was added to the chlorides solution, and stirred overnight. The resulting milky solution turned transparent upon addition of 7 mL of water containing 324 mg of NH_4F. After further vigorous stirring for 30 min, the solution was introduced in the Teflon insert (50 mL) of a pressure digestion vessel (DAB-2, Berghof). The reactor was then introduced in an oven and kept at 180 °C for 5 h. After this time, the synthesized nanoparticles were recovered from the solution by centrifugation (5500 rpm, 12 min), and then redispersed in water, sonicated, and washed twice by centrifugation. The particles are kept in water solution at 1.3 mg/mL or 0.7 mg/mL of Nd^{3+} concentration (measured through ICP).

Assembly of gold nanostars and Ln^{3+}-doped nanoparticles to polystyrene beads

0.5mL of PEG-stabilized AuNS solution 0.1 mM or 0.5 mM was added dropwise onto 100 µL of PS beads (0.25 % in solid in 0.1 M NaCl) in an Eppendorf tube under sonication during 5 min and then, 0.5 mL of Ln^{3+}-doped NPs (0.1 M NaCl solution) was added and sonicated 5 min and the particle mixture was incubated overnight. Two different Ln^{3+}-doped nanoparticles concentrations (1.3 mg/mL or 0.7 mg/mL of Nd^{3+}) were used to obtain different luminescence loading. The unbound nanoparticles were removed by two centrifugation steps (2000 rpm, 4 min, 20 °C) and the samples were redispersed in Milli-Q water. TEM images of hybrid beads individually modified with each type of nanoparticle, as well as of the full structure, are shown in Figure S3. Figure S4 shows several images of the beads loaded

with different concentrations of nanoparticles. In Figure S5 we show the absorbance spectra of the gold nanostars alone and in the final beads. The main difference observed in the lower wavelength range is due to scattering of the beads, meaning that the plasmonic resonance of the stars is not strongly modified during the synthesis, which would happen if their shape is changed or if they aggregate.

Silica coating AuNSs/CaF_2:Nd^{3+},Y^{3+} immobilized polystyrene beads

Silica coating of the assembled beads was carried out by diluting 200 µL of an aqueous dispersion of beads in a mixture of 1 mL of water and 1.8 mL of isopropanol. With this solution in a 5 mL glass vial and under stirring, 18 µL of ammonia (32%) was added, to set the pH between 9 and 10. After further stirring over 30 min, 50 µL of additional CaF_2:Nd^{3+},Y^{3+} (0.3 w/w %) was added, to enhance the luminescent character of the assembly. The solution was then sonicated for ten minutes, and stirred for 20 more minutes. Afterwards, 200 µL of TEOS solution in isopropanol (2 w/w %) was added. The mix was left stirring overnight, and finally, the particles were washed by centrifugation three-fold (2000 rpm, 10 min) to recover the resulting silica coated beads that can be redispersed either in water or in cell media. In addition to the images shown in Figure 2C and D, representative images of the coated beads are included in Figure S6.

The concentration of each type of particle in the beads was measured through ICP, both with the hybrid beads dispersed in water and in the cell media (EMEM). The CaF_2:Au ratio in the final assembly was determinedto be 20:1 in mass (though it varies a bit between samples and can be as low as 10:1 or as high as 30:1, depending on the starting concentrations used). This means that there are around 700 CaF_2 nanoparticles per gold nanostar, which makes sense given the small volume of CaF_2 nanoparticles compared to that of gold nanostars.

3D cell culture

Experiments in cells were performed using U-87MG (epithelial, human glioblastoma cancer) as a model cell line. The cells were cultured in EMEM cell media completed with a 10% fetal bovine serum (FBS) and 1% antibiotics (penicillin and streptomycin, PS), all purchased from Invitrogen. To prepare spheroids, the selected number of starting cells (either 5000 or 10000) were plated in the well of an ultra-low attachment U-bottom 96-well plate (Nexcelom bioscience) in 200uL of complete cell media. The cells naturally group at the center of the well, forming a rounded cluster after 24H (day 1) that becomes a compact spheroid after 48H (day 2), and can now be easily handled. The size and shape evolution of the spheroids is shown in Figure S8.

To treat the spheroids, a concentrated solution of hybrid beads in water was diluted in EMEM (with 10% FBS) to reach the desired concentration. The final volume of water was always kept below 25 % of the total volume, as we determined that the effect of water on the viability of spheroids wasn´t detrimental at that concentration. The spheroids were then cultured in 200 uL of this solution. This step was always done after 60H (at the end of day 2) of life of the spheroid. The spheroids were incubated like that for 48H to let the particles internalize before doing any further experiment.

Spheroid fluorescence imaging: Lightsheet microscope

Preparation of spheroids for imaging

In order to image spheroids in the Lightsheet microscope, they need to be fixed, stained and mounted in agar matrix. The followed protocol started with washing the spheroids by keeping them in PBS for 10 min while gentle shaking was applied. This process was repeated three times. They were then fixed by immersing them in a solution of paraformaldehyde (2% in PBS). The spheroids were kept in this solution for 2 hours, in which they stayed on a rocking shaker at 4 ^oC. Afterwards, the spheroids where washed again in PBS, this time the process was repeated three times in 5 min cycles. Once the spheroids were fixed, they were stained with DAPI. In order to do so, they were kept in a 16 µM solution of DAPI in PBS. This step was done at room temperature, in complete darkness and for 40 min. Then, the spheroids where washed in PBS twice, 10 min per cycle. The spheroids where then mounted in low melting agarose to be imaged, paying attention to the temperature of the agarose, that was 35^oC when the spheroids where added to it.

When required, propidium iodide (PI) staining was done before fixation, but after the first washing cycles in PBS. In order to do so, spheroids where immersed for 20 min in a 1 mg/mL solution of PI in PBS. After this process, spheroids where washed twice in PBS, and the preparation protocol for Lightsheet microscopy continued as explained above.

Imaging technique

To image cell spheroids, a Lightsheet microscope (Zeiss, Lightsheet Z.1) was used. DAPI fluorescence was excited at 405 nm and its emission detected using a bandpass filter (420 – 470 nm). To use the luminescence of Nd^{3+} to locate the particles, Nd^{3+} was excited with the 561 nm laser line of the microscope

and its luminescence was recorded in the near-infrared range. In order to remove any autofluorescence background, the microscope was manipulated to incorporate a longpass filter (Thorlabs, cut-off 850 nm).

Propidium iodide (PI) has been occasionally applied to study the proportion of live and dead cells in spheroids. Its use was restricted in most experiments, since the luminescent signal of this dye creates a background that hinders the signal from Nd^{3+}. However, we judged important to understand the composition of the spheroids in terms of cell life before proceeding with the experiments (Figure S9).

Routine characterization techniques

Transmission electron microscopy (TEM) images were obtained in a JEOL JEM-2100F electron microscope, at an acceleration voltage of 120 kV. Samples for TEM analysis were prepared by adding a single drop (2 µL) of the aqueous solution (ca. 0.1 mg/mL in milliQ water) of particles onto a copper grid coated with a carbon film (Electron Microscopy Sciences). Further details on the preparation of grids are added to the SI, Section A4.

UV-Vis spectra were measured in an Agilent 8453 UV-Vis diode-array spectrophotometer. Zeta potential measurements were performed in a Malvern Zetasizer 3000 HS particle size analyzer (Malvern Instruments, UK). Fluorescence measurements were carried out with a PerkinElmer LS55 Fluorescence Spectrometer. ICP-MS measurements were performed on a Thermo iCAP Q ICP-MS (Thermo Fisher Scientific GmbH, Bremen, Germany). A ASX560 autosampler was coupled to the ICP-MS (CETAC Tech, Omaha, NE, USA). In order to digest the different materials for ICP experiments, 100 µL of CaF_2 particles aqueous solution was digested overnight in 10 mL HNO_3 (65%, Scharlau) at 70 ^oC. Full beads were digested overnight in aqua regia. Spheroids were digested in aqua regia as well, but they required sonication before and after a 24H digestion time.

Optical Set-up and Hyperthermia Experiments

Optical characterization of the emission of $CaF_2:Nd^{3+},Y^{3+}$ nanoparticles was done by illuminating the sample at 808 nm with a fiber-coupled laser diode (Lumics, LU808T040), with the beam collimated to a 3 mm diameter spot. Emission was collected by a lens, filtered (longpass filter, Thorlabs, cut-off 850 nm) to remove any laser signal, and then recorded by an InGaAs spectrometer (Sol 1.7, B&WTek).

Hyperthermia experiments were performed in the same way, keeping the spheroids in a 200 µL well with quartz bottom (to avoid any luminescent signal from the well) that was illuminated from top (Figure 3A). Laser light was not blocked just after the well, but two centimeters later, avoiding like this any possible heating due to the light absorbance of the materials constituting the set-up. During the experiments, spheroids were kept in the well with 180 µL of cell media, and were moved to the incubator just after the treatment. Aiming to obtain further information from the spheroids and the effect of the treatment, a portable microscope (Aven, Mighty Scope 1.3M, 175x) was used to acquire images of the different samples before and immediately after the treatments.

To study the viability of the spheroids CellTiter-glo 3D test (Promega) has been used, always 24H after the treatment.

Raman spectra

During the experiments, the Raman spectra of water had to be recorded. To do so, a Renishaw inVia Raman Reflex microscope was used.

Supplementary Material

Supplementary figures and tables.
http://www.thno.org/v09p7298s1.pdf

Acknowledgements

M.Q. and L.M.L.-M. acknowledge financial support from the European Commission under the Marie Sklodowska-Curie program (H2020-MSCA-IF-2014_659021 - PHELLINI). L.M.L.-M. acknowledges funding by the European Research Council (ERC Advanced Grant 787510, 4DBioSERS). This work was performed under the Maria de Maeztu Units of Excellence Program from the Spanish State Research Agency – Grant No. MDM-2017-0720. R.G.A. acknowledges partial support of this work through a CIC biomaGUNE - University of Manchester Collaborative Research Programme.

The authors would like to acknowledge Blanca Arnaiz, who kindly donated U87MG cells. M.Q. would like to acknowledge Judith Langer for her support with Raman spectroscopy.

Competing Interests

The authors have declared that no competing interest exists.

References

1. Evans SS, Repasky EA, Fisher DT. Fever and the thermal regulation of immunity: the immune system feels the heat. Nat Rev Immunol. 2015; 15: 335-49.
2. Jaque D, Martinez Maestro L, del Rosal B, Haro-Gonzalez P, Benayas A, Plaza JL, et al. Nanoparticles for photothermal therapies. Nanoscale. 2014; 6: 9494-530.
3. Leuenberger P, Ganscha S, Kahraman A, Cappelletti V, Boersema PJ, von Mering C, et al. Cell-wide analysis of protein thermal unfolding reveals determinants of thermostability. Science. 2017; 355: eaai7825.

4. Hobohm U. Healing Heat: Harnessing infection to fight cancer. American Scientist. 2009; 97: 34.
5. Cruz MM, Ferreira LP, Alves AF, Mendo SG, Ferreira P, Godinho M, et al. Chapter 19 - Nanoparticles for magnetic hyperthermia. In: Ficai A, Grumezescu AM, Eds. Nanostructures for Cancer Therapy. United Kingdom: Elsevier; 2017. p. 485-511.
6. Espinosa A, Kolosnjaj-Tabi J, Abou-Hassan A, Plan Sangnier A, Curcio A, Silva AKA, et al. Magnetic (Hyper)Thermia or Photothermia? Progressive Comparison of Iron Oxide and Gold Nanoparticles Heating in Water, in Cells, and In Vivo. Adv Funct Mater. 2018; 28: 1803660.
7. Geng B, Yang D, Pan D, Wang L, Zheng F, Shen W, et al. NIR-responsive carbon dots for efficient photothermal cancer therapy at low power densities. Carbon. 2018; 134: 153-62.
8. Song AS, Najjar AM, Diller KR. Thermally Induced Apoptosis, Necrosis, and Heat Shock Protein Expression in Three-Dimensional Culture. J Biomech Eng. 2014; 136: 071006--10.
9. Rock KL, Kono H. The inflammatory response to cell death. Annu Rev Pathol: Mech Dis. 2008; 3: 99-126.
10. Spirou SV, Costa Lima SA, Bouziotis P, Vranješ-Djurić S, Efthimiadou EK, Laurenzana A, et al. Recommendations for In Vitro and In Vivo Testing of Magnetic Nanoparticle Hyperthermia Combined with Radiation Therapy. Nanomaterials. 2018; 8: 306 (31).
11. Fratila RM, De La Fuente Martinez J, editors. Nanomaterials for Magnetic and Optical Hyperthermia Applications. Amsterdam (Netherlands): Elsevier; 2019.
12. Quintanilla M, Liz-Marzán LM. Guiding Rules for Selecting a Nanothermometer. Nano Today. 2018; 19: 126-45.
13. Carlos LD, Palacio F, editors. Thermometry at the Nanoscale. Techniques and Selected Applications. Cambridge, UK: Royal Society of Chemistry; 2016.
14. Shi L, Sordillo LA, Rodríguez-Contreras A, Alfano R. Transmission in near-infrared optical windows for deep brain imaging. J Biophotonics. 2016; 9: 38-43.
15. Wang FF, Wan H, Ma ZR, Zhong YT, Sun QC, Tian Y, et al. Light-sheet microscopy in the near-infrared II window. Nat Methods. 2019; 16: 545-552.
16. Editorial. Seeing red. Nat Methods. 2017; 14: 637.
17. Laissue PP, Alghamdi RA, Tomancak P, Reynaud EG, Shroff H. Assessing phototoxicity in live fluorescence imaging. Nat Methods. 2017; 14: 657-61.
18. Li Z, Lopez-Ortega A, Aranda-Ramos A, Tajada JL, Sort J, Nogues C, et al. Simultaneous Local Heating/Thermometry Based on Plasmonic Magnetochromic Nanoheaters. Small. 2018; 14: 1800868.
19. Rocha U, Kumar KU, Jacinto C, Ramiro J, Caamaño AJ, Solé JG, et al. Nd^{3+} doped LaF_3 nanoparticles as self-monitored photo-thermal agents. Appl Phys Lett. 2014; 104: 053703.
20. del Rosal B, Carrasco E, Ren F, Benayas A, Vetrone F, Sanz-Rodríguez F, et al. Infrared-Emitting QDs for Thermal Therapy with Real-Time Subcutaneous Temperature Feedback. Adv Funct Mater. 2016; 26: 6060-8.
21. Suo H, Zhao X, Zhang Z, Guo C. 808 nm Light-Triggered Thermometer–Heater Upconverting Platform Based on Nd^{3+}-Sensitized Yolk–Shell GdOF@SiO_2. ACS Appl Mater Interfaces. 2017; 9: 43438-48.
22. Bednarkiewicz A, Wawrzynczyk D, Nyk M, Strek W. Optically stimulated heating using Nd^{3+} doped $NaYF_4$ colloidal near infrared nanophosphors. Appl Phys B. 2011; 103: 847-52.
23. Piñol R, Brites CDS, Bustamante R, Martínez A, Silva NJO, Murillo JL, et al. Joining Time-Resolved Thermometry and Magnetic-Induced Heating in a Single Nanoparticle Unveils Intriguing Thermal Properties. ACS Nano. 2015; 9: 3134-42.
24. Debasu ML, Brites CDS, Balabhadra S, Oliveira H, Rocha J, Carlos LD. Nanoplatforms for Plasmon-Induced Heating and Thermometry. ChemNanoMat. 2016; 2: 520-7.
25. Huang Y, Skripka A, Labrador-Paez L, Sanz-Rodriguez F, Haro-Gonzalez P, Jaque D, et al. Upconverting nanocomposites with combined photothermal and photodynamic effects. Nanoscale. 2018; 10: 791-9.
26. Chen X, Xia Q, Cao Y, Min Q, Zhang J, Chen Z, et al. Imaging the transient heat generation of individual nanostructures with a mechanoresponsive polymer. Nat Commun. 2017; 8: 1498.
27. Dias JT, Moros M, del Pino P, Rivera S, Grazú V, de la Fuente JM. DNA as a Molecular Local Thermal Probe for the Analysis of Magnetic Hyperthermia. Angew Chem Int Ed. 2013; 52: 11526-9.
28. Riley RS, Day ES. Gold nanoparticle-mediated photothermal therapy: applications and opportunities for multimodal cancer treatment. Wiley Interdiscip Rev Nanomed Nanobiotechnol. 2017; 9: 1-24.
29. M. Maestro L, Haro-Gonzalez P, Sanchez-Iglesias A, Liz-Marzan LM, García Solé J, Jaque D. Quantum Dot Thermometry Evaluation of Geometry Dependent Heating Efficiency in Gold Nanoparticles. Langmuir. 2014; 30: 1650-8.
30. Baffou G, Quidant R, Girard C. Heat generation in plasmonic nanostructures: Influence of morphology. Appl Phys Lett. 2009; 94: 153109 (1-3).
31. Yuan H, Khoury CG, Hwang H, Wilson CM, Grant GA, Vo-Dinh T. Gold nanostars: surfactant-free synthesis, 3D modelling, and two-photon photoluminescence imaging. Nanotechnology. 2012; 23: 075102-.
32. Pedroni M, Piccinelli F, Passuello T, Polizzi S, Ueda J, Haro-Gonzalez P, et al. Water (H_2O and D_2O) Dispersible NIR-to-NIR Upconverting Yb^{3+}/Tm^{3+} Doped MF_2 (M = Ca, Sr) Colloids: Influence of the Host Crystal. Cryst Growth Des. 2013; 13: 4906-13.
33. Quintanilla M, Zhang Y, Liz-Marzán LM. Subtissue Plasmonic Heating Monitored with CaF_2:Nd^{3+},Y^{3+} Nanothermometers in the Second Biological Window. Chem Mater. 2018; 30: 2819-28.
34. Serrano-Montes AB, Langer J, Henriksen-Lacey M, Jimenez de Aberasturi D, Solís DM, Taboada JM, et al. Gold Nanostar-Coated Polystyrene Beads as Multifunctional Nanoprobes for SERS Bioimaging. J Phys Chem C. 2016; 120: 20860-8.
35. Chen Y-S, Frey W, Kim S, Homan K, Kruizinga P, Sokolov K, et al. Enhanced thermal stability of silica-coated gold nanorods for photoacoustic imaging and image-guided therapy. Opt Express. 2010; 18: 8867-78.
36. Hanske C, Sanz-Ortiz MN, Liz-Marzan LM. Silica-Coated Plasmonic Metal Nanoparticles in Action. Adv Mater. 2018; 30: 1707003.
37. Khoury CG, Vo-Dinh T. Gold Nanostars For Surface-Enhanced Raman Scattering: Synthesis, Characterization and Optimization. J Phys Chem C. 2008; 112: 18849-59.
38. Artlett CP, Pask HM. Optical remote sensing of water temperature using Raman spectroscopy. Opt Express. 2015; 23: 31844-56.
39. Hu Q, Lü X, Lu W, Chen Y, Liu H. An extensive study on Raman spectra of water from 253 to 753 K at 30 MPa: A new insight into structure of water. I Mol Spectrosc. 2013; 292: 23 - 7.
40. Zanoni M, Piccinini F, Arienti C, Zamagni A, Santi S, Polico R, et al. 3D tumor spheroid models for in vitro therapeutic screening: a systematic approach to enhance the biological relevance of data obtained. Sci Rep. 2016; 6: 19103.
41. Balabhadra S, Debasu ML, Brites CDS, Ferreira RAS, Carlos LD. Upconverting Nanoparticles Working As Primary Thermometers In Different Media. J Phys Chem C. 2017; 121: 13962-8.
42. Quintanilla M, Cantelar E, Cusso F, Villegas M, Caballero AC. Temperature sensing with up-converting submicron-sized $LiNbO_3$:Er^{3+}/Yb^{3+} particles. Appl Phys Express. 2011; 4: 022601.
43. Vanrompay H, Bladt E, Albrecht W, Béché A, Zakhozheva M, Sánchez-Iglesias A, et al. 3D characterization of heat-induced morphological changes of Au nanostars by fast in situ electron tomography. Nanoscale. 2018; 10: 22792-801.
44. Rohani S, Quintanilla M, Tuccio S, de Angelis F, Cantelar E, Govorov AO, et al. Enhanced luminescence, collective heating and nanothermometry in an ensemble system composed of lanthanide-doped upconverting nanoparticles and gold nanorods. Adv Opt Mater. 2015; 3: 1606-13.
45. Richardson HH, Carlson MT, Tandler PJ, Hernandez P, Govorov AO. Experimental and Theoretical Studies of Light-to-Heat Conversion and Collective Heating Effects in Metal Nanoparticle Solutions. Nano Lett. 2009; 9: 1139-46.
46. Roper DK, Ahn W, Hoepfner M. Microscale Heat Transfer Transduced by Surface Plasmon Resonant Gold Nanoparticles. The journal of physical chemistry C, Nanomaterials and interfaces. 2007; 111: 3636-41.
47. Yi PN, Alexander CR, Fenn JO, Jarrett JH, Lung B, Wallace KM, et al. Swelling of multicellular spheroids induced by hyperthermia. International Journal of Hyperthermia. 1987; 3: 217-33.